

# Structural and Electrochemical Properties of the High Ni Content Spinel LiNiMnO<sub>4</sub>

Tianyi Li<sup>1</sup>, Kai Chang<sup>1</sup>, Ahmed M. Hashem<sup>2,\*</sup>, Ashraf E. Abdel-Ghany<sup>2</sup>, Rasha S. El-Tawil<sup>2</sup>, Hua Wang<sup>1</sup>, Hazim El-Mounayri<sup>1</sup>, Andres Tovar<sup>1</sup>, Likun Zhu<sup>1,\*</sup> and Christian M. Julien<sup>3,\*</sup>

<sup>1</sup> Department of Mechanical and Energy Engineering, Indiana University Purdue University Indianapolis, Indianapolis, IN 46202, USA; tl41@iupui.edu (T.L.); kc59@iu.edu (K.C.); wanghua@iu.edu (H.W.); helmouna@iupui.edu (H.E.-M.); tovara@iupui.edu (A.T.)

<sup>2</sup> Inorganic Chemistry Department, National Research Centre, 33 El Bohouth St., (former El Tahrir St.), Dokki-Giza 12622, Egypt; achraf\_28@yahoo.com (A.E.A.-G.); r2samir@yahoo.com (R.S.E.-T.)

<sup>3</sup> Institut de Minéralogie, de Physique des Matériaux et Cosmologie (IMPMC), Sorbonne Université, UMR-CNRS 7590, 4 Place Jussieu, 75752 Paris, France

\* Correspondence: ahmedh242@yahoo.com (A.M.H.); likzhu@iupui.edu (L.Z.); christian.julien@sorbonne-universite.fr (C.M.J.)

## 1. Experimental: synthesis (EDTA-assisted sol-gel method) and coin cell assembly

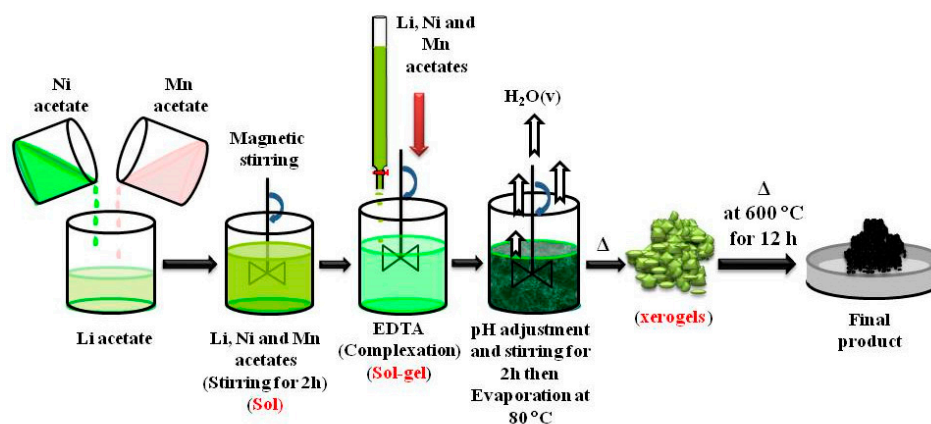


**Figure S1.** Schematic representation of the synthesis of Li-Ni-Mn-O spinel materials using the EDTA-assisted sol-gel method with subsequent annealing at moderate temperature.

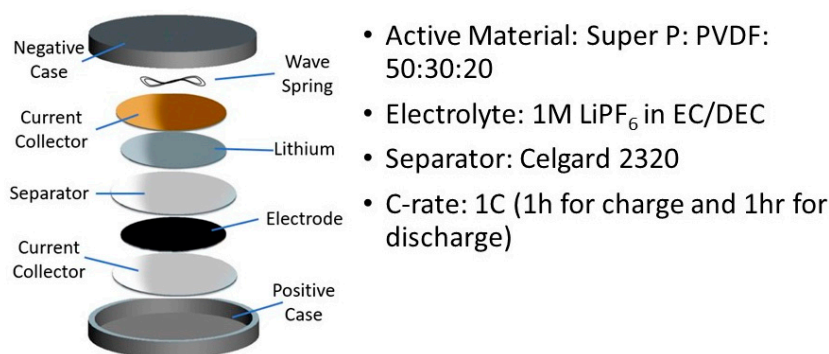


**Figure S2.** Schematic representation of the coin-cell assembly. Note that the low coating ratio of active material (50 wt.%) and low mass loading of the electrode 1.5 mg/cm<sup>2</sup> are definitely increase the electrode's stability as well as the ability of electrode to cycling at high current density.

## 2. Surface morphology the spinel electrodes

The positive electrode composite was fabricated through a slurry composed of active material, conducting Super-P carbon black and poly(vinylidene fluoride) (PVdF) binder in the proportion 50:30:20 casted onto Al foil as current collector. The size of the electrode disc is 12 mm in diameter with a mass loading of 1.5 mg cm<sup>-2</sup>. Based on the SEM images, we are barely found any morphological differences between the LiNi<sub>y</sub>Mn<sub>2-y</sub>O<sub>4</sub> materials. The differences in the cycling performance are due to Ni doping not particle variations.

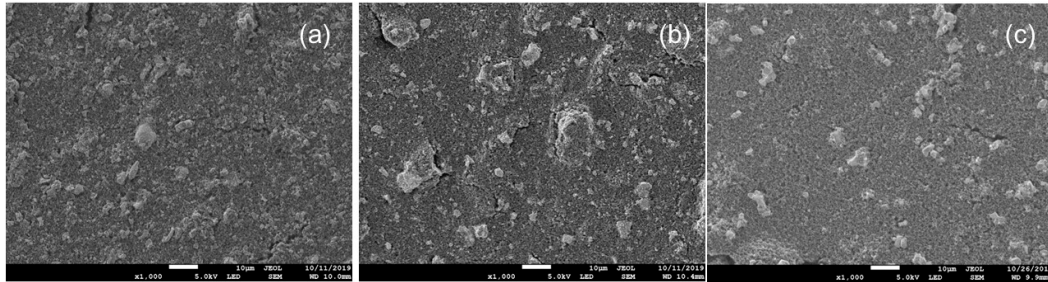


**Figure S3.** SEM images of electrodes fabricated using the slurry composed of active material, conducting Super-P carbon black and PVdF binder. (a) LiMn<sub>2</sub>O<sub>4</sub>, (b) LiNi<sub>0.5</sub>Mn<sub>1.5</sub>O<sub>4</sub> and (c) LiNiMnO<sub>4</sub>@NMO. The scale bar is 1 μm.

## 3. BET isotherms

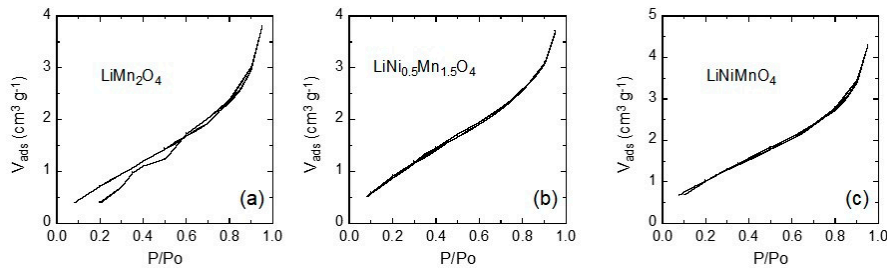


**Figure S4.** Nitrogen adsorption/desorption isotherms for (a) LiMn<sub>2</sub>O<sub>4</sub>, (b) LiNi<sub>0.5</sub>Mn<sub>1.5</sub>O<sub>4</sub> and (c) LiNiMnO<sub>4</sub>@NMO.

## 4. Raman spectroscopy

In the wavenumber range investigated (120-800), the RS spectrum of LiMn<sub>2</sub>O<sub>4</sub> (LMO) displays six active modes, which match well with the spectral features of the  $Fd\bar{3}m$  spinel structure as the group factor analysis of the  $O_h$  symmetry provides the  $A_{1g} + E_g + 3T_{2g}$  spectroscopic species. These vibrations are located at 164, 386, 473, 582, 621 and 654 cm<sup>-1</sup>, respectively (Figure S4a) [1]. The strong band around 600 cm<sup>-1</sup> is viewed as the symmetric Mn–O stretching vibration involving motion of oxygen atoms inside the MnO<sub>6</sub> octahedron, which is split at 582 cm<sup>-1</sup> ( $A_{1g}^{(1)}$  mode) and 621 cm<sup>-1</sup> ( $A_{1g}^{(2)}$  mode) because the presence of regular Mn<sup>IV</sup>O<sub>6</sub> and distorted Mn<sup>III</sup>O<sub>6</sub> octahedra. The peaks at 386 and 473 cm<sup>-1</sup> are attributed to the  $E_g$  and  $T_{2g}^{(2)}$  mode, respectively, while the high-frequency  $T_{2g}^{(3)}$  mode is observed at 654 cm<sup>-1</sup>. The low-frequency band at 164 cm<sup>-1</sup> is an external mode assigned to the translational vibration  $T_{2g}^{(1)}$ .

The Raman spectrum of LiNi<sub>0.5</sub>Mn<sub>1.5</sub>O<sub>4</sub> (LNM) is more complicated than that of LMO because the substitution of Ni<sup>2+</sup> for Mn<sup>3+</sup> in the spinel lattice. In particular, the introduction of nickel leads to increased number of vibration bands and Raman intensity of certain modes. The spectrum displays 10 vibrational modes located at 163, 220, 343, 403, 496, 525, 597, 610, 636 and 665 cm<sup>-1</sup>. Attribution of these Raman patterns are reported in Figure S4b and in Table S1 [2]. However, it is worthy to note that: (i) the doubling of the  $A_{1g}$  mode (at 610 and 636 cm<sup>-1</sup>) due to the presence of cations Mn<sup>3+</sup> and Mn<sup>4+</sup>, (ii) the splitting of modes into several components due to the partial substitution, i.e.,  $T_{2g}(T)$  at 163 and 220 cm<sup>-1</sup>.

<sup>1</sup>,  $T_{2g}^{(2)}$  at 496 and 525 and  $A_{1g}$  at 597 and 610  $\text{cm}^{-1}$ . Of specific vibrations of Ni-O bonds can thus be identified at 496, 525 and 597  $\text{cm}^{-1}$ . It is also not excluded that nickel participates in the intensity high  $A_{1g}$  mode located at 640  $\text{cm}^{-1}$ . No splitting is observed for the  $E_g$  and  $T_{2g}^{(3)}$  modes located at 403 and 665  $\text{cm}^{-1}$ , respectively, and which probably contain in their large envelope the contributions of the Ni and Mn atoms.

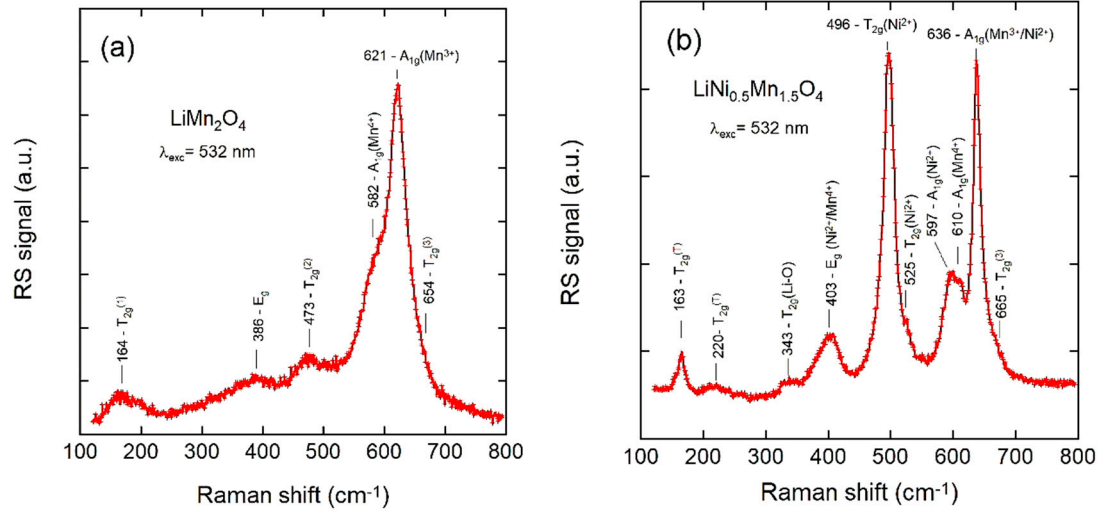


**Figure S5.** Raman spectra recorded with the excitation line at  $\lambda = 532 \text{ nm}$  of (a)  $\text{LiMn}_2\text{O}_4$  and (b)  $\text{LiNi}_{0.5}\text{Mn}_{1.5}\text{O}_4$  spinels.

**Table S1.** Raman mode attribution for  $\text{LiMn}_2\text{O}_4$ ,  $\text{LiNi}_{0.5}\text{Mn}_{1.5}\text{O}_4$   $\text{LiNiMnO}_4$ @NMO. w : weak, m : medium, s : strong, vs: very strong, b :broad.

$\text{LiMn}_2\text{O}_4$	Attribution	$\text{LiNi}_{0.5}\text{Mn}_{1.5}\text{O}_4$	$\text{LiNiMnO}_4$ @NMO	Attribution
164 m	$T_{2g}^{(1)}$	163 m	164 m	$T_{2g}^{(1)}$
-		220 b	-	$T_{2g}^{(1)}$
-		343 b	341 b	$T_{2g}(\text{Li-O})$
389 b	$E_g$	403 b	412 b	$E_g(\text{Ni}^{2+}/\text{Mn}^{4+})$
473 m	$T_{2g}^{(2)}$	496 s	499 s	$T_{2g}(\text{Ni}^{2+})$
-		525 w	520 w	$T_{2g}(\text{Ni}^{2+})$
582 s	$A_g^{(1)}$	597 m	599 m	$A_{1g}(\text{Ni}^{2+})$
-		610 m	612 m	$A_{1g}(\text{Mn}^{4+})$
621 s	$A_g^{(2)}$	636 s	637 w	$A_{1g}(\text{Mn}^{3+}/\text{Ni}^{2+})$
654 w	$T_{2g}^{(3)}$	665 w	667 w	$T_{2g}^{(3)}$

## 5. XPS measurements

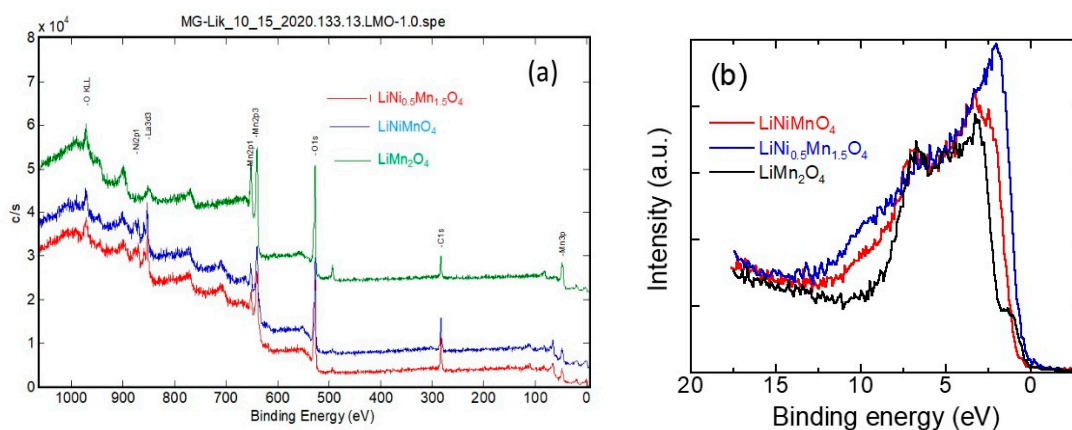


**Figure S6.** XPS characterization of LMP, LNM and LNM@NMO spinel powders synthesized by sol-gel method: (a) Survey spectra, (b) XPS valence band spectra.

## 6. Electrochemical performance of LMO and LNM

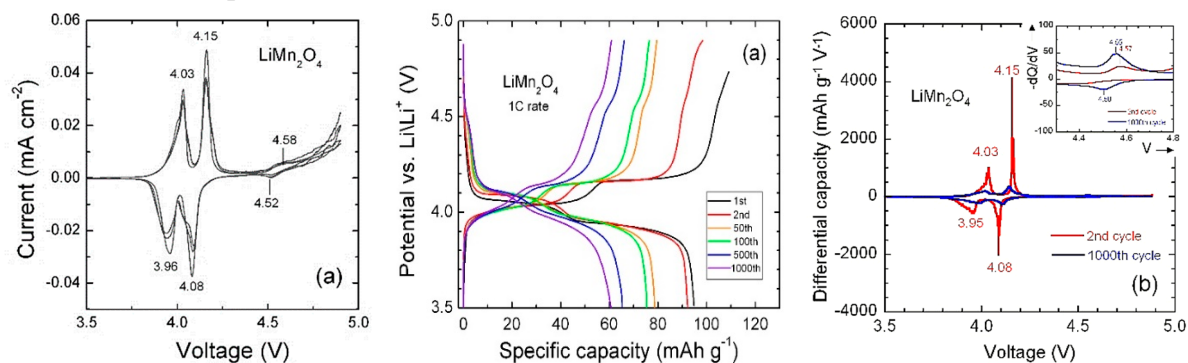


**Figure S7.** Electrochemical performance of  $\text{LiMn}_2\text{O}_4$ . (a) Cyclic voltammograms (three cycles) recorded at the scan rate of  $0.02 \text{ mV s}^{-1}$ . (b) Galvanostatic charge-discharge profiles carried out at  $148 \text{ mA g}^{-1}$  current rate in the potential window 3.5-4.9 V. (c) Differential capacity ( $-dQ/dV$ ) vs. potential of the  $\text{LiNi}_{0.5}\text{Mn}_{1.5}\text{O}_4$  electrode in  $1 \text{ mol L}^{-1}$   $\text{LiPF}_6$  in EC:DEC (1:1) electrolyte.

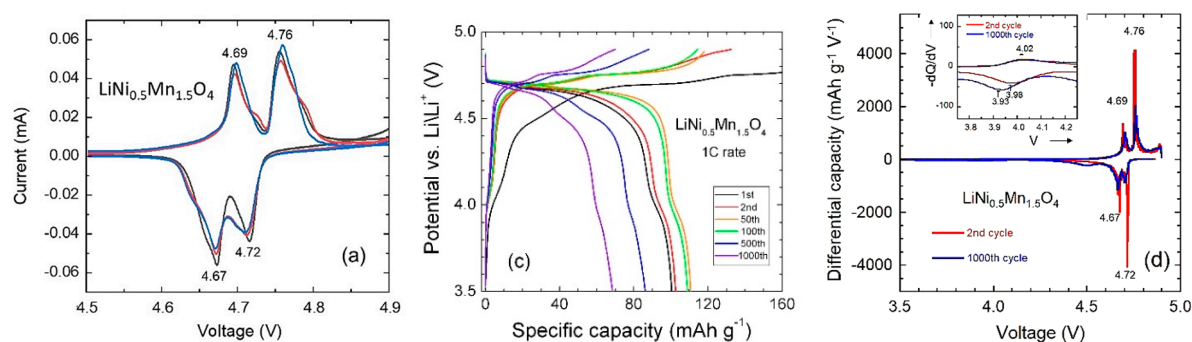


**Figure S8.** Electrochemical performance of  $\text{LiNi}_{0.5}\text{Mn}_{1.5}\text{O}_4$ . (a) Cyclic voltammograms (three cycles) recorded at the scan rate of  $0.02 \text{ mV s}^{-1}$ . (b) Galvanostatic charge-discharge profiles carried out at  $148 \text{ mA g}^{-1}$  current rate in the potential window 3.5-4.9 V. (c) Differential capacity ( $-dQ/dV$ ) vs. potential of the  $\text{LiNi}_{0.5}\text{Mn}_{1.5}\text{O}_4$  electrode in  $1 \text{ mol L}^{-1}$   $\text{LiPF}_6$  in EC:DEC (1:1) electrolyte.

**Table S2.** Electrochemical performance upon long-term cycling of LNM cathode materials synthesized by different methods. The discharge capacity of fresh LNM//Li cells and that after cycling is documented. The relevant cycle number is given in brackets.

Synthesis	Discharge capacity (mAh g <sup>-1</sup> )	Current rate (mA g <sup>-1</sup> )	Ref.
Co-precipitation	128/80	14.8 (250)	[3]
Combustion (citric acid) <sup>a)</sup>	70/48	148 (1000)	[4]
Sol-gel (citric acid assisted)	130/50	14.8 (500)	[5]
Co-precipitation	70/30	700 (500)	[6]
Planetary ball milling	85/50	1480 (500)	[7]
Solid-state reaction	110/70	70 (1000)	[8]
Spray pyrolysis	102/94	140 (500)	[9]
Solid-state reaction	130/33	70 (350)	[10]
Co-precipitation	110/75	140 (1000)	[11]
Sol-gel (EDTA assisted)	110/70	140 (1000)	this work

<sup>a)</sup> LiNi<sub>0.15</sub>Mg<sub>0.08</sub>Mn<sub>1.77</sub>O<sub>4</sub> composition.

## References

- Julien, C.M.; Massot, M. Lattice vibrations of materials for lithium rechargeable batteries I. Lithium manganese oxide spinel. *Mater. Sci. Eng. B* **2003**, *97*, 217–230.
- Zhu, W.; Liu, D.; Trottier, J.; Gagnon, C.; Howe, J.; Mauger, A.; Julien, C.M.; K. Zaghib, K. In-situ Raman spectroscopic investigation of LiMn<sub>1.45</sub>Ni<sub>0.45</sub>M<sub>0.1</sub>O<sub>4</sub> (M = Cr, Co) 5 V cathode materials. *J. Power Sources* **2015**, *298*, 341–348.
- Börner, M.; Niehoff, P.; Vortmann, B.; Nowak, S.; Winter, M.; Schappacher, F.M. Comparison of different synthesis methods for LiNi<sub>0.5</sub>Mn<sub>1.5</sub>O<sub>4</sub>—Influence on battery cycling performance, degradation, and aging, *Energy Technol.* **2016**, *4*, 1631-1640.
- Yu, Y.; Guo, J.; Xiang, M.; Su, C.; Liu, X.; Bai, H.; Bai, W.; Duan, K. Enhancing the durable performance of LiMn<sub>2</sub>O<sub>4</sub> at high-rate and elevated temperature by nickel magnesium dual doping. *Sci. Rep.* **2019**, *9*, 16864.
- Li, L.; Zhao, R.; Xu, T.; Wang, D.; Pan, D.; Zhang, K.; Yu, C.; Lu, X.; He, G.; Bai, Y. Stabilizing a high-voltage LiNi<sub>0.5</sub>Mn<sub>1.5</sub>O<sub>4</sub> cathode towards all solid state batteries: a Li–Al–Ti–P–O solid electrolyte nano-shell with a host material. *Nanoscale* **2019**, *11*, 8967-8977.
- Yin, C.; Zhou, H.; Yang, Z.; Li, J. Synthesis and electrochemical properties of LiNi<sub>0.5</sub>Mn<sub>1.5</sub>O<sub>4</sub> for Li-ion batteries by the metal–organic framework method. *ACS Appl. Mater. Interfaces* **2018**, *10*, 13625–13634.
- Wang, H.; Shi, Z.; Li, J.; Yang, S.; Ren, R.; Cui, J.; Xiao, J.; Zhang, B. Direct carbon coating at high temperature on LiNi<sub>0.5</sub>Mn<sub>1.5</sub>O<sub>4</sub> cathode: Unexpected influence on crystal structure and electrochemical performances. *J. Power Sources* **2015**, *288*, 206–213.
- Fang, X.; Ge, M.; Rong, J.; Zhou, C. Graphene-oxide-coated LiNi<sub>0.5</sub>Mn<sub>1.5</sub>O<sub>4</sub> as high voltage cathode for lithium ion batteries with high energy density and long cycle life. *J. Mater. Chem. A* **2013**, *1*, 4083–4088.
- Wang, J.; Nie, P.; Jiang, J.; Wu, Y.; Fu, R.; Xu, G.; Zhang, Y.; Dou H.; Zhang, X. High-voltage Li<sub>2</sub>SiO<sub>3</sub>–LiNi<sub>0.5</sub>Mn<sub>1.5</sub>O<sub>4</sub> hollow spheres prepared through in situ aerosol spray pyrolysis towards high-energy Li-ion batteries. *Chem. Electro. Chem.* **2018**, *5*, 1212–1218.
- Chong, J.; Xun, S.; Zhang, J.; Song, X.; Xie, H.; Battaglia V.; Wang, R. Li<sub>3</sub>PO<sub>4</sub>-Coated LiNi<sub>0.5</sub>Mn<sub>1.5</sub>O<sub>4</sub>: A stable high-voltage cathode material for lithium-ion batteries. *Chem.–Eur. J.* **2014**, *20*, 7479–7485.
- Lu, D.; Yuan, L.; Chen, Z.; Zeng, R.; Cai, Y. Co-precipitation preparation of LiNi<sub>0.5</sub>Mn<sub>1.5</sub>O<sub>4</sub> hollow hierarchical microspheres with superior electrochemical performance for 5 V Li-ion batteries. *J. Alloys Compd.* **2018**, *730*, 509–515.